Alfven Instability in coronal loops with siphon flows

Taroyan, Youra

Published in:
Astrophysical Journal

DOI:
10.1088/0004-637X/694/1/69

Publication date:
2009

Citation for published version (APA):
Taroyan, Y. (2009). Alfven Instability in coronal loops with siphon flows. *Astrophysical Journal*, *694*(1), 69-75. https://doi.org/10.1088/0004-637X/694/1/69

The Astrophysical Journal, 694:69–75, 2009 March 20 doi:10.1088/0004-637X/694/1/69

ALFVÉN INSTABILITY IN CORONAL LOOPS WITH SIPHON FLOWS

Y. Taroyan
Department of Applied Mathematics, University of Sheffield, Sheffield S3 7RH, UK; Y.Taroyan@sheffield.ac.uk
Received 2008 September 12; accepted 2008 December 15; published 2009 March 13

ABSTRACT

A new magnetohydrodynamic (MHD) instability in coronal loops is presented. It is demonstrated that small-amplitude torsional Alfvénic disturbances generated by random photospheric motions are inevitably amplified in asymmetrically stratified loops with siphon flows. The loop asymmetry and the flow speeds can be arbitrarily small. The growth rates linked with the instability increase with increasing flow speeds. The instability is caused by over-reflection of Alfvén waves at the transition region where steep variations in density exist.

Key words: instabilities – MHD – Sun: atmosphere

Online-only material: color figure

1. INTRODUCTION

Plasma flows are a common feature of various solar coronal structures and may have important dynamic and energetic implications. Despite the great difficulties associated with accurate flow measurements, many attempts have been made to analyze data obtained from different instruments (Cushman & Rense 1976; Rottman et al. 1982; Mariska & Dowdy 1992; Neupert et al. 1992; Brekke et al. 1997). Co-aligned *Transition Region and Coronal Explorer* (*TRACE*) and Solar Ultraviolet Measurement of Emitted Radiation (SUMER) observations by Winebarger et al. (2002) revealed steady line-of-sight flows of up to 40 km s^{-1} in active region loops which appear static in *TRACE* images. Doyle et al. (2006) carried out similar co-aligned observations to detect transient flows of up to 120 km s^{-1} in cool loops. Recently, attempts have been made to analyze flow patterns in loop structures using the EUV Imaging Spectrometer (EIS) instrument onboard the new Hinode satellite (Doschek et al. 2007; Del Zanna 2008; Hara et al. 2008).

Various aspects of subsonic and supersonic unidirectional steady flows in coronal loops have been studied by employing one-dimensional loop models. Such models are described by the set of hydrodynamic equations along the loop coordinate. Motions in other directions are ignored. Solutions with subsonic speeds throughout the loop are often called siphon flow solutions. Siphon flows in coronal loops can be driven by various mechanisms such as overpressure at one footpoint, asymmetric heating or asymmetric loop cross sections (Cargill & Priest 1980; Mariska & Boris 1983; Craig & McClymont 1986; Thomas 1988; Orlando et al. 1995).

Coronal loops in active regions observed with *TRACE* and EIT show enhanced densities, enhanced pressure scale heights, and flat filter ratio profiles in comparison with the predictions of static-equilibrium theory (Aschwanden et al. 2000). Patsourakos et al. (2004) and Petrie (2006) argued that the observed features could not be reproduced by one-dimensional loop models with steady siphon flows.

Recent observations with CoMP and Hinode/Solar Optical Telescope (Hinode/SOT) indicate the presence of transverse Alfvén waves in various solar atmospheric structures from chromospheric spicules to prominences and X-ray jets (Tomczyk et al. 2007; Cirtain et al. 2007; De Pontieu et al. 2007; Okamoto et al. 2007). The nature of the detected waves has been debated (Erdélyi & Fedun 2007; Terradas et al. 2008; Van Doorsselaere et al. 2008). Transverse waves with flows in coronal loops were reported by Ofman & Wang (2008).

Torsional Alfvén waves have been studied in static structures both in the context of coronal heating (Hollweg et al. 1982; Kudoh & Shibata 1999; Moriyasu et al. 2004; Antolin et al. 2008) and coronal seismology (Ofman 2002; Gruszecki et al. 2007; Zaqarashvili & Murawski 2007). It has been proposed that the energy required to maintain the loops at high coronal temperatures is supplied by large amplitude Alfvén waves which are nonlinearly converted into slow and fast MHD waves. These waves subsequently steepen into shocks and dissipate. The process is most efficient when the base-to-apex expansion of the loop cross-sectional area is large. Other possible mechanisms of heat deposition include resonant absorption (Ionson 1978; see also De Groof et al. 2002; De Groof & Goossens 2002) and phase mixing (Heyvaerts & Priest 1983). Alfvén waves are launched into the corona either monochromatically (Belien et al. 1999) or by a random driver (Moriyasu et al. 2004) from photospheric/chromopheric heights. In both cases, the average amplitude of the driver needs to be larger than 1 km s^{-1} in order to balance the losses. It has been estimated that such large amplitude Alfvén waves are unlikely to be generated at photospheric heights (Parker 1991).

The present paper presents a previously unknown mechanism for the amplification of torsional Alfvén waves in coronal loops which does not require large amplitude drivers at the footpoints of the loops. Also no large area expansion factors are needed. The energy required for wave amplification is extracted from the mass flow and is proportional to its speed. The mechanism is based on a new linear MHD instability which we call the *Alfvén instability*. Among other well-known instabilities in ideal MHD are the sausage and kink instabilities. Such instabilities are important as they modify the large-scale structure and dynamics of the plasma. The Alfvén instability does not require the mass flow to have a shear which makes it different from the well-known shear flow instabilities. A necessary condition for the existence of the Alfvén instability is the presence of a magnetic field permeated by a *compressible* flow.

2. MODEL AND GOVERNING EQUATIONS

Figure 1 represents the model. A coronal loop shown at the top is straightened and divided into three regions: the ± regions

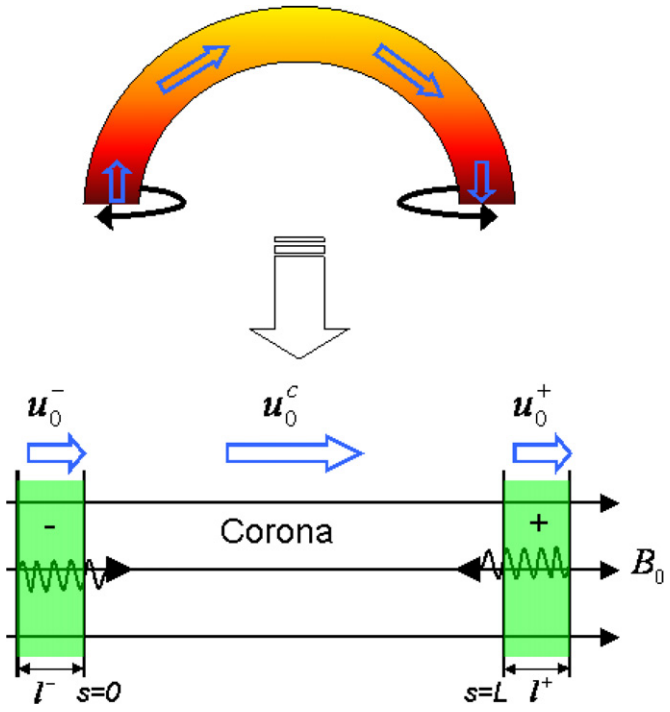

Figure 1. Coronal loop permeated by a siphon flow (top) is straightened and divided into three regions (bottom): the ± regions with lengths $l^{\pm}$ representing the lower photosphere/chromosphere environment and the coronal part of the loop stretching from $s = 0$ to $s = L$, where s is the coordinate along the magnetic field. Torsional Alfvénic disturbances driven by convective motions of the footpoints travel through the loop along the field lines.

(A color version of this figure is available in the online journal.)

representing the dense photosphere/chromosphere environment and the middle region representing the corona. The magnetic field is uniform with a constant magnitude of B_0 in all the three regions. The coordinate along the field lines is denoted by s. There is a steady siphon flow along the loop from one footpoint to the other. Arbitrary torsional Alfvénic disturbances with small amplitudes are launched at the loop footpoints by convection. The subsequent evolution of these disturbances along the entire loop is governed by the azimuthal components of the linearized MHD equations of motion and induction:

$$\rho_0 \frac{\partial v}{\partial t} + \rho_0 u_0 \frac{\partial v}{\partial s} = \frac{B_0}{\mu_0} \frac{\partial b}{\partial s},$$
$$\frac{\partial b}{\partial t} + u_0 \frac{\partial b}{\partial s} = B_0 \frac{\partial v}{\partial s} - b \frac{\partial u_0}{\partial s}, \quad (1)$$

where u_0, ρ_0 denote the equilibrium flow speed and density, and v, b are the perturbations of the azimuthal velocity and magnetic field. Using the equation of mass continuity, $\rho_0 u_0 = \text{const}$, we reduce the set of Equations (1) into a single second-order partial differential equation for the variable b:

$$\frac{\partial^2 b}{\partial t^2} + 2\frac{\partial^2}{\partial t \partial s}(u_0 b) + \frac{\partial}{\partial s}\left(u_0 \frac{\partial}{\partial s}\left(\frac{u_0^2 - c_A^2}{u_0} b\right)\right) = 0, \quad (2)$$

where the Alfvén speed $c_A(s) = B_0/(\mu_0 \rho_0(s))^{1/2}$ has been introduced. It is assumed that the flow speed is sub-Alfvénic throughout the loop. The variables v, b are set proportional to $\exp(-i\omega t)$:

$$v = \tilde{v} \exp(-i\omega t), \quad b = \tilde{b} \exp(-i\omega t), \quad (3)$$

where ω is the frequency. For simplicity, the tildes will be omitted in the forthcoming analysis. The substitution of Equation (3) for b transforms Equation (2) into

$$\left(u_0^{j\,2} - c_A^{j\,2}\right) \frac{d^2 b}{ds^2} - 2i\omega u_0^j \frac{db}{ds} - \omega^2 b = 0, \quad (4)$$

where the superscript symbol j indicates the corresponding equilibrium quantity in either of the three regions shown in Figure 1: $j = -$ for $-l^- < s < 0$, $j = c$ (corona) for $0 < s < L$ and $j = +$ for $L < s < L + l^+$. The solution of Equation (4) in each region j is given by the formula

$$b = A^j \exp \frac{i\omega s}{u_0^j + c_A^j} + B^j \exp \frac{i\omega s}{u_0^j - c_A^j}, \quad (5)$$

where the first/second term represents the wave component propagating toward the right/left footpoint. The governing equation cast in the form of Equation (2) enables us to connect Solutions (5) across the interfaces $s = 0, L$. First, the magnetic field perturbation b must be continuous. The second connection formula follows from Equation (2) and the continuity of b. Thus, we have

$$\{b\} = 0, \quad \left\{\left(u_0^2 - c_A^2\right)\frac{db}{ds} - 2i\omega u_0 b\right\} = 0, \quad (6)$$

where the braces denote the jump of the enclosed quantity across an interface.

An apparent physical interpretation of Equations (6) can be given by introducing the wave energy flux as

$$\mathbf{S} = \mathbf{e} \times \mathbf{b}, \quad (7)$$

where $\mathbf{e} = -\mathbf{v} \times \mathbf{B_0} - \mathbf{u_0} \times \mathbf{b}$ is the electric field perturbation. By making use of Lagrange's formula for triple vector products and expressing the variable v in terms of b, we can express the nonvanishing s component of the Poynting vector (7) in the form

$$S = 2u_0^j b^2 - \frac{1}{i\omega}\left(u_0^{j\,2} - c_A^{j\,2}\right) b \frac{db}{ds}. \quad (8)$$

Equations (6) therefore express the continuity of the energy density and the energy flux associated with the Alfvén waves.

The coefficients A^j, B^j are to be determined from the boundary conditions at the footpoints $s = -l^-, L + l^+$ and from the connection formulae (6) at $s = 0, L$. The resulting set of six algebraic equations can be written in the following matrix form:

$$\mathcal{A}\mathbf{X} = \mathbf{I}, \quad (9)$$

where the vectors $\mathbf{X}$ and $\mathbf{I}$ are given by

$$\mathbf{X} = \begin{pmatrix} A^- \\ B^- \\ A^c \\ B^c \\ A^+ \\ B^+ \end{pmatrix}, \quad \mathbf{I} = \begin{pmatrix} I^- \\ 0 \\ 0 \\ 0 \\ 0 \\ I^+ \end{pmatrix}, \quad (10)$$

and the matrix $\mathcal{A}$ is defined in the appendix. The vector components I^-, I^+ are arbitrary and represent the driver at the corresponding footpoint.

Several previous studies of Alfvén waves in static loops focused on resonances resulting from monochromatic driving

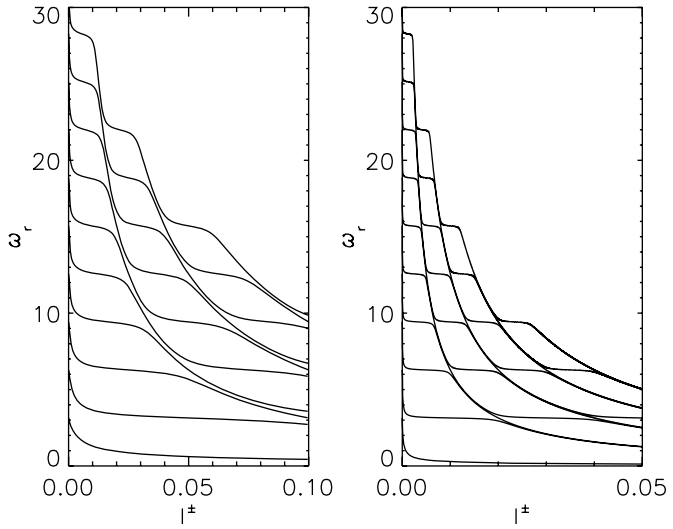

Figure 2. First 10 Alfvénic eigenfrequencies in a loop with no flow. The left panel is for $c_A^{\pm} = 0.1$ and the right panel is for $c_A^{\pm} = 0.02$. In both cases, the horizontal axis represents the length of the lower $\pm$ regions with $l^+ = l^-$.

at one footpoint with close/open boundaries at the other footpoint (Ionson 1982; Hollweg 1984a, 1984b). In general, convective motions are expected to result in random forcing of the footpoints with a broad frequency spectrum (see, e.g., Hollweg 1982; Kudoh & Shibata 1999; Moriyasu et al. 2004). Upon inversion into the time domain, the singularities in the frequency domain will be smoothed out and the motion will remain linear (assuming a small-amplitude driver).

In addition to having a new feature, namely, a siphon flow, the present model is not restricted to any particular forcing terms I^-, I^+. It also contains parameters l^- and l^+ which can be altered from 0 to ∞ to mimic various boundaries.

The solution of the original equation $b(t, s)$ can be decomposed into a linear combination of terms like $\exp(-i\omega_n t)$, where ω_n are the poles of $b(\omega, s)$ in the complex ω plane. According to Equation (9), the coefficients $\mathbf{X}$ are given by the formula $\mathbf{X} = \mathcal{A}^{-1}\mathbf{I}$. Therefore, the solution $b(\omega, s)$ of the Laplace-transformed equation and its inverse $b(t, s)$ depend on the zeros of $\det \mathcal{A}$ in the complex ω plane. The zeros of $\det \mathcal{A}$ represent the eigenfrequencies and determine the evolution of the system in response to arbitrary torsional perturbations at the footpoints. After some algebra, the condition $\det \mathcal{A} = 0$ is reduced to the following transcendental equation:

$$\exp \frac{2i\omega c_A^c L}{\left(u_0^c - c_A^c\right)\left(u_0^c + c_A^c\right)} = \mathcal{R}_0^c \mathcal{R}_L^c, \tag{11}$$

where $\mathcal{R}_0^c$ and $\mathcal{R}_L^c$ are defined in the appendix.

3. ANALYSIS OF THE ALFVÉN MODES

The system described by Equation (11) has an infinite number of eigenmodes. Any perturbation can be described by a superposition of these eigenmodes. In general, the eigenfrequency $\omega = \omega_r + i\omega_i$ is complex. According to the adopted notation (3), $\omega_i > 0$ corresponds to instability and $\omega_i < 0$ corresponds to damping. Note that Equation (11) is reduced to

$$\exp \frac{2i\omega c_A^c L}{\left(u_0^c - c_A^c\right)\left(u_0^c + c_A^c\right)} = 1 \tag{12}$$

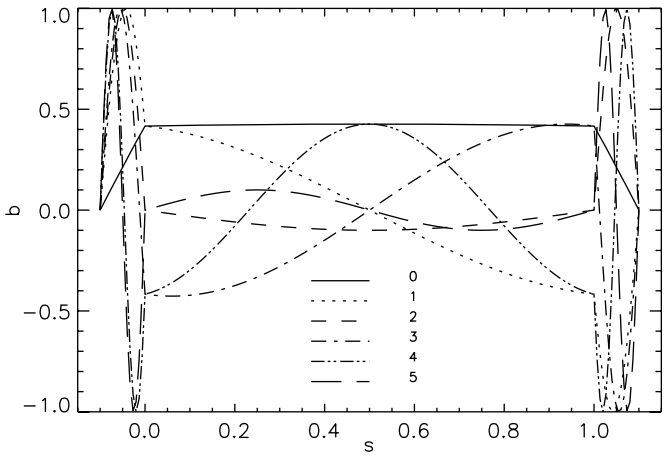

Figure 3. Spatial structure of the first six eigenmodes corresponding to the eigenfrequencies plotted in Figure 2 (left panel) with $|l^{\pm}| = 0.1$. The numbered lines indicate the fundamental mode (solid line) and its harmonics.

when $l^{\pm} = 0$, i.e., when the lower atmosphere is neglected. The analytical solutions of Equation (12) are given by

$$\omega = \frac{\left(u_0^c - c_A^c\right)\left(u_0^c + c_A^c\right)\pi n}{c_A^c L}, n = 0, \pm 1, \pm 2, \ldots \tag{13}$$

and the modes are stable. Equation (11) always permits a trivial solution.

For nonzero $l^{\pm}$, Equation (11) is solved numerically using Newton's method. In the forthcoming analysis, the dependence of the nontrivial eigenfrequencies on various parameters of the system is examined. Length is normalized with respect to L, and speed is normalized with respect to c_A^c.

3.1. Stable Modes in a Loop with a Static Plasma

In order to get a picture of the eigenmode structure, we first examine the case when the flow is absent. It is assumed that $l^- = l^+$. The dependence of the first 10 eigenfrequencies on l^- is plotted in Figure 2. The eigenfrequencies do not have imaginary parts and therefore only the real parts are shown. The lowest curve represents the fundamental mode. Note that it differs from the fundamental mode of a loop with no lower regions. According to Equation (13), the frequency of the latter is given by $\omega = c_A^c \pi / L$. Meanwhile, in the present situation, the frequency of the fundamental mode is much lower due to the added travel time in the $\pm$ regions, where the Alfvén speed is low. The mode number increases with increasing frequency. Figure 2 displays many avoided crossings between different modes. These crossings indicate interaction between the Alfvén waves propagating in the corona (the frequencies of which approximately represent horizontal lines determined by Equation (12)) and their counterparts in the $\pm$ regions. A more insightful interpretation of the interaction at the two interfaces in terms of wave reflection and transmission will be presented in Section 5.

The normalized eigenfunctions corresponding to the first six eigenfrequencies (Figure 2, left panel) are plotted in Figure 3. Different modes are marked with different numbers. Each of these indicates the number of corresponding nodes along the loop. For example, the fundamental mode represented by the solid line has no crossings with the horizontal axis inside the loop. Figure 3 shows that the spatial profiles of the eigenmodes differ from what would be expected for a loop with a constant

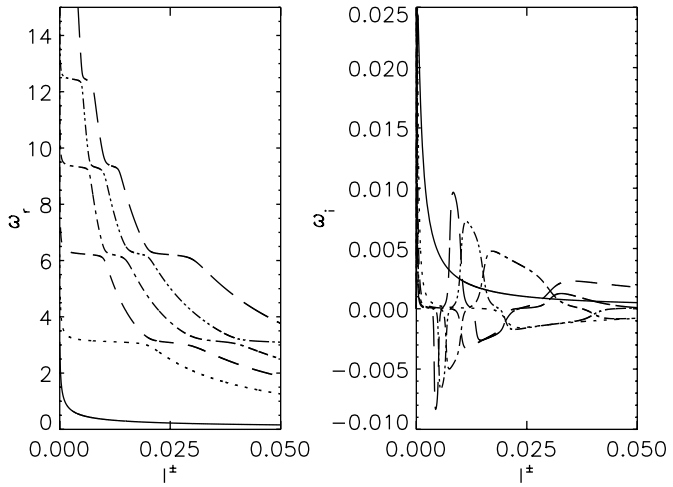

Figure 4. Real and imaginary frequencies of the first six Alfvén modes plotted as functions of $l^{\pm}$ where $l^{+} = l^{-}$. The Alfvén speed in the loop is asymmetric: $c_A^{-} = 0.03$ and $c_A^{+} = 0.02$. The flow speed in the coronal part $u_0^c = 0.1$.

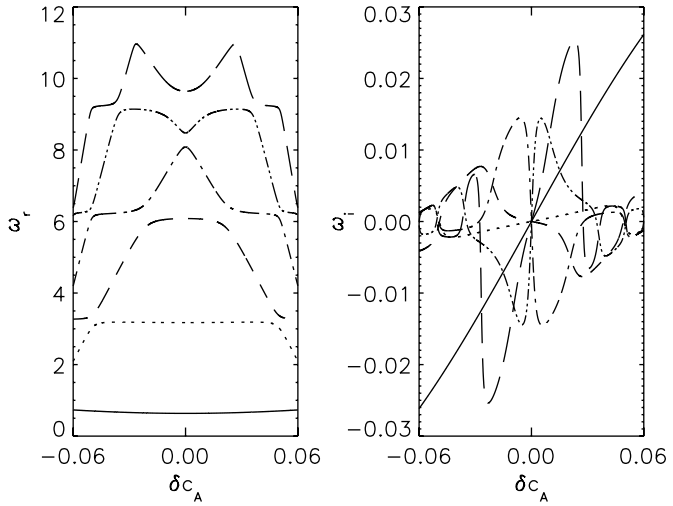

Figure 5. Dependence of the frequencies and growth rates on the Alfvén speed difference defined by expressions (15). The first six modes are plotted with different lines. The length of the ± regions is $l^{\pm} = 0.03$ and the coronal flow speed is fixed at $u_0^c = 0.1$.

Alfvén speed. Considering the background Alfvén speed profile along the loop, the relative amplitudes are larger in ± regions. The amplitudes of even modes ($n = 0, 2, \ldots$) still have local maxima at the apex, whereas the amplitudes of odd modes have local minima.

3.2. Unstable Modes in a Loop with a Siphon Flow

Next, the eigenmodes are analyzed when the loop is permeated by a steady flow of plasma from one footpoint to the other. In deriving Equation (11), no assumption was made regarding the flow direction. It is therefore possible to examine effects of both negative and positive flows. Using the equation of mass continuity, we may express the flow speeds in the ± regions through their coronal counterpart:

$$u_0^{\pm} = u_0^c \left(\frac{c_A^{\pm}}{c_A^c} \right)^2 . \tag{14}$$

In the following discussion, the coronal flow speed u_0^c is normalized with respect to c_A^c. As it will become clear, the instability arises when, in addition to the flow, the loop contains some kind of asymmetry. Two different cases of loop asymmetry are examined: different Alfvén speeds and different lengths of the ± regions.

3.2.1. Loops with Asymmetric Alfvén Speed ($c_A^{-} \neq c_A^{+}$)

Figure 4 shows that in a loop with a siphon flow the Alfvén modes have both real (ω_r) and imaginary (ω_i) frequencies. Some of the modes are damped corresponding to $\omega_i < 0$, others are amplified with $\omega_i > 0$ leading to an instability. Only the first six modes are shown. Different modes are indicated with different lines. The curve with the lowest real frequency corresponds to the fundamental mode. It has a growth rate which rapidly increases and gradually decays as $l^{\pm}$ increases.

The dependence of the frequencies and growth rates on the difference between the Alfvén speeds is plotted in Figure 5. As δc_A increases, the Alfvén speeds change according to

$$c_A^{\pm} = 0.08 \mp \delta c_A . \tag{15}$$

The first six modes are shown in Figure 5. The instability only disappears when the loop is perfectly symmetric so that $\delta c_A = 0$. In general, the growth rates tend to increase with increasing difference between the Alfvén speed in the − region and its counterpart in the + region.

3.2.2. Loops with Geometric Asymmetry ($l^{-} \neq l^{+}$)

We now assume that the Alfvén speed is the same in the ± regions. The loop asymmetry is geometric. The variation of the real and imaginary parts of ω with increasing Alfvén speed $c_A^{\pm}$ is plotted in Figure 6. Depending on the value of $c_A^{\pm}$, a given mode can be either damped or amplified. However, the instability is always present and the growth rates tend to be larger when $l^{+} > l^{-}$.

The dependence of the complex eigenfrequencies on the coronal flow speed u_0^c is displayed in Figure 7. The plots are for the first seven eigenmodes. Figure 7 shows that there are unstable modes for both negative and positive values of the argument. The modes become stable and undamped only when the flow is absent. The instability does not require any lower nonzero threshold speed to set in. The growth rates, in general, tend to increase with increasing flow speed.

4. OVER-REFLECTION OF ALFVÉN WAVES AT THE TRANSITION REGION

In order to understand the physical nature of the instability, we use the concept of wave reflection. The reflection coefficient is usually defined as the ratio of the outgoing and incident wave amplitudes at a given interface. In the above-presented results, each mode is a combination of two waves traveling in opposite directions. The amplitudes of these waves can be calculated using Equations (5). In such a way, the reflection coefficient is calculated for every single mode. The coronal reflection coefficient at $s = 0$ is given by the ratio A^c/B^c, where the ω-dependent amplitudes A^c and B^c are defined in Equations (5). After some algebra, we find that the coronal reflection coefficient at $s = 0$ is equal to $|\mathcal{R}_0^c|$, where $\mathcal{R}_0^c$ figures in Equation (11) and is defined in the appendix. In a similar way, it can be shown that the coronal reflection coefficient at $s = L$ is equal to $|\mathcal{R}_L^c|$. Therefore, the modulus of Equation (11)

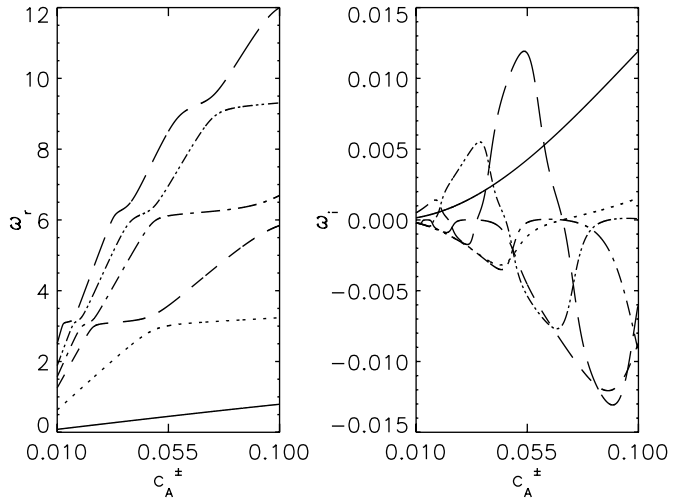

Figure 6. Complex frequencies of the first six modes plotted as functions of $c_A^{\pm}$. The coronal flow speed is fixed at $u_0^c = 0.1$ and the lengths of the regions $\pm$ are fixed at $l^- = 0.02$ and $l^+ = 0.05$.

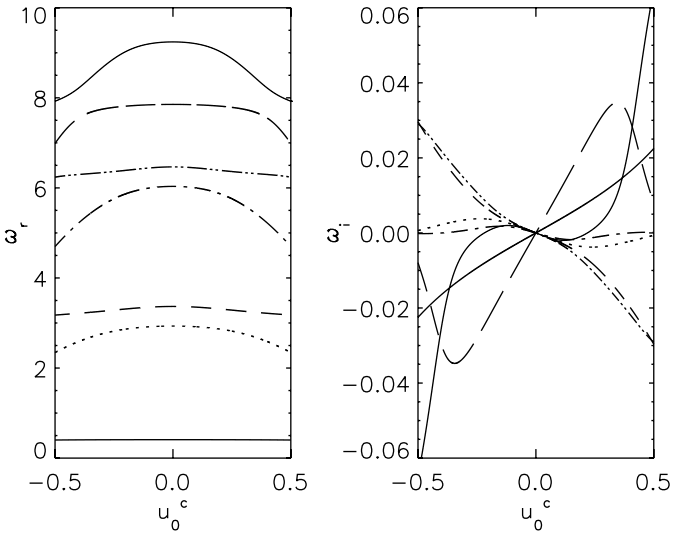

Figure 7. Dependence of the first seven complex eigenmode frequencies on the coronal flow speed u_0^c. The Alfvén speed in the loop is symmetric: $c_A^{\pm} = 0.05$. The $\pm$ regions have different lengths: $l^- = 0.02$ and $l^+ = 0.05$.

is nothing else but the net reflection of Alfvén waves into the corona. These two coefficients are plotted separately in Figure 8. Only results for the first seven modes are shown. The waves are partially reflected at $s = L$ when the flow is in the negative direction. On the other hand, the reflection coefficient $|\mathcal{R}_0^c|$ is greater than 1. This means that the waves are *over-reflected* at $s = 0$. The concept of over-reflection was first introduced by Miles (1957) and McKenzie (1970) for acoustic and MHD waves in shear flows. As the flow speed approaches zero, the reflection coefficients $|\mathcal{R}_0^c|, |\mathcal{R}_L^c| \to 1$ and the eigenmodes are stable and undamped. When the flow speed becomes positive, the reflection coefficients $|\mathcal{R}_0^c|$ and $|\mathcal{R}_L^c|$ exchange their roles: the waves are partially reflected at $s = 0$ and over-reflected at $s = L$. According to Equation (11), net over-reflection in the corona ($|\mathcal{R}_0^c \mathcal{R}_L^c| > 1$) corresponds to instability ($\omega_i > 0$), whereas partial reflection corresponds to damping. According to Figure 7, there are always modes for which net over-reflection into the corona occurs whenever there is a siphon flow.

The arguments set out above can be extended and applied to the $\pm$ regions. First, we introduce a reflection coefficient $|\mathcal{R}_0^-|$ at $s = 0$ in the region $-$ as the amplitude ratio B^-/A^-. In a similar way, a reflection coefficient $|\mathcal{R}_L^+|$ at $s = L$ in the region $+$ is introduced. It can be shown that

$$|\mathcal{R}_0^-| = \exp \frac{2\omega_i c_A^- l^-}{(c_A^- - u_0^-)(c_A^- + u_0^-)},$$
$$|\mathcal{R}_L^+| = \exp \frac{2\omega_i c_A^+ l^+}{(c_A^+ - u_0^+)(c_A^+ + u_0^+)}. \quad (16)$$

The above-derived expressions for $|\mathcal{R}_0^-|$ and $|\mathcal{R}_L^+|$ show that instabilities occur whenever the Alfvén waves are over-reflected at $s = 0, L$ into the $-$ and $+$ regions. In other words, $\omega_i > 0$ if $|\mathcal{R}_0^-| > 1$, $|\mathcal{R}_L^+| > 1$, and vice versa.

In view of the presented physical arguments, we conclude that the instability is a result of over-reflection into the $\pm$ regions and into the corona. The over-reflection and the conversion of flow energy into wave energy take place at the interfaces $s = 0$ and $s = L$. These interfaces with steep density variations represent the transition region and upper chromosphere. According to Figure 8, waves traveling in the corona are over-reflected at $s = L$ and partially reflected at $s = 0$ when the flow speed is positive. The loop asymmetry provides imbalance between $|\mathcal{R}_0^c|$ and $|\mathcal{R}_L^c|$ so that the net reflection into the corona is different from 1. According to Equation (11), the modes are amplified ($\omega_i > 0$) in the case of net over-reflection $|\mathcal{R}_0^c \mathcal{R}_L^c| > 1$ and damped otherwise. For a symmetrically stratified loop, the reflection coefficients $|\mathcal{R}_0^c|$, $|\mathcal{R}_L^c|$ balance each other and the modes remain stable.

5. IMPLICATIONS OF THE ALFVÉN INSTABILITY

In one-dimensional loop modeling, it has been customary to assume that dynamic processes eventually settle into a near-stationary state, so that the hydrodynamic equations yield time-independent steady flow solutions. A steady siphon flow usually requires some kind of asymmetry in the system (see references in Section 1). An important consequence of the present study is that a near-stationary state cannot be reached if the footpoints are randomly disturbed by torsional motions. Such disturbances will exponentially grow in time by exchanging energy with the flow. The problem can no longer be treated in one dimension even if the driver amplitudes are small. As the Alfvénic disturbances grow in time, they could nonlinearly transfer their energy to longitudinal motions and thus make the flow unsteady.

Persistent red shifts corresponding to downflows have long been observed in transition region lines (Doschek et al. 1976; Peter & Judge 1999; Doyle et al. 2002). Figure 8 shows that a negative gradient in the flow causes over-reflection and hence acts as a source of wave energy, whereas a positive gradient acts as a sink of energy. Therefore, upflows in both legs of a loop caused by chromospheric evaporation are likely to act as a sink of wave energy due to positive flow gradients. On the other hand, downflows in both legs will lead to enhanced energy exchange and growth of the Alfvénic disturbances which could account for the temporal variability of the observed Doppler shifts (Doyle et al. 2002).

Peter (2001) used data from the SUMER spectrometer on-board *Solar and Heliospheric Observatory* to study the structure and dynamics of the upper chromosphere and transition

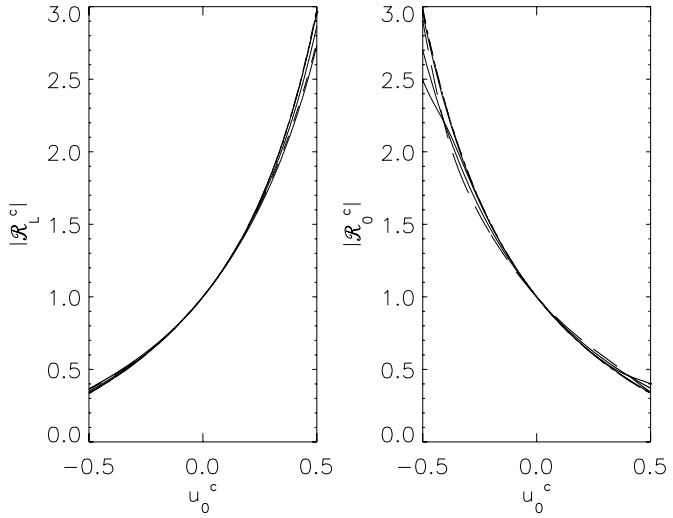

Figure 8. Reflection coefficients of Alfvén waves in the corona at $s = L$ (left panel) and $s = 0$ (right panel). The dependence of the reflection coefficients on the flow speed in the corona is shown for the first seven eigenmodes. The values of the parameters are the same as in Figure 7.

region. Rather large nonthermal broadenings were observed in several lines. Peter (2001) argued that a most likely explanation for such broadenings could be Alfvén waves passing through the footpoints (funnels) of coronal loops. The waves were estimated to be nonlinear with an average 10% amplitude of the background Alfvén speed. Considering the ubiquity of field-aligned flows in the chromosphere and transition region (for example, spicules), it does not seem unlikely that these nonlinear waves are generated by the presented instability mechanism. According to Figure 3, the ratio of the amplitudes to the background Alfvén speed must be largest in the lower regions.

It must be emphasized that the Alfvén instability does not necessarily lead to formation of coherent waves. However, individual wave modes are expected to be observed if the corresponding growth rates are dominant. Figure 4 presents such an example: the fundamental mode (solid line) grows fastest for small values of $l^{\pm}$ that correspond to long loops. Using the parameter values in Figure 4, we may estimate the e-folding time τ_e, i.e., the time required for the amplitude to increase by a factor of e. For a fixed value of $l^{\pm} = 0.02$, the ratio of the frequency and the growth rate corresponding to the fundamental mode (solid line in Figure 4) is $\omega_r/\omega_i \approx 70$. Therefore, the expected e-folding time measured in oscillation periods is $\tau_e = \omega_r/(2\pi\omega_i) \approx 10$: it would take about 10 periods for the oscillation to grow by a factor of e. Ofman & Wang (2008) have recently detected fundamental mode transverse oscillations in a long loop using Hinode/SOT. The loop was permeated by a plasma flow of about 100 km s^{-1} consistent with the value used in Figure 4. Despite the large uncertainties, weak damping or even growth of the oscillation amplitude was observed for three periods. The above-derived e-folding time could be applicable to the loop presented in that paper. However, our estimates are likely to change for a loop model with a more realistic geometry and density structuring in the lower parts of the atmosphere.

The aim of the present paper is to present an application of a new ideal MHD instability in the solar atmosphere. A more detailed analysis is required to get better insight into the energetic and dynamic consequences of the Alfvén instability. Future work must take into account (1) the loop expansion in the lower regions that may affect the flow profile and modify the governing equations; (2) the nonlinear and resonant coupling to compressional modes in the presence of inhomogeneities; (3) effects of loop curvature and gravity. Ultimately, in the future, one could study an initial value problem in which the torsional disturbances at photospheric levels, outflows/inflows along the footpoints of the loops and their expansion factors are taken as an input from observations with very high resolution instruments.

6. SUMMARY

A loop model with a steady siphon flow is studied. The loop is divided into three regions: a dense photosphere/chromosphere environment near the two footpoints (− and +) with a tenuous corona in the middle. In general, the − and + regions are allowed to have different densities and lengths. It is assumed that the loop is shaken randomly at the footpoints by convective motions which generate small-amplitude torsional Alfvén waves traveling along the loop in both directions. The response of the loop to such footpoint perturbations depends on the temporal behavior of its eigenmodes. Solutions in each region are derived and connected using the continuity of the magnetic field and the Poynting flux. The system has an infinite number of eigenmodes, and only the first few are examined in detail. In the absence of a flow, the modes are stable and the disturbances remain linear.

The inclusion of a siphon flow significantly modifies the loop response. It is shown that in asymmetric loops with siphon flows some of the eigenmodes are damped, others are unstable. Two different cases of loop asymmetry are examined: density asymmetry and geometric asymmetry between the − and + regions. For flows in the positive direction, the growth rates tend to become larger when the Alfvén travel time l^+/c_A^+ in the + region is longer than the corresponding counterpart in the − region. The reverse is true for flows in the negative direction. No critical flow speeds are required for the instability to set in. In general, the growth rates increase with increasing flow speeds.

The new MHD instability is interpreted in terms of wave over-reflection. It is shown that the growth/damping rates of the eigenmodes are intrinsically linked with the reflection coefficients at the two interfaces that separate the three regions. These interfaces represent the transition region where the density steeply decreases from chromospheric to coronal values. The presence of a siphon flow in an asymmetric loop inevitably leads to a previously unknown ideal MHD instability which is due to over-reflection of Alfvén waves at the transition region. This allows us to identify the transition region as the location of energy exchange between the flow and the Alfvén waves.

The present study only examines the first few unstable modes for a range of loop parameters. Therefore, we can only speculate on the energetic and dynamic implications of this new instability. A future study must concentrate on the nonlinear evolution of the instability for specific loop parameters. The chromosphere must be separated from the photosphere and a more realistic density profile must be adopted. It is also important to take into account the effects of variable loop cross sections, loop curvature and gravity. Finally, the applicability of the new instability mechanism to compressional MHD waves could be studied.

The author is grateful to the Leverhulme Trust for financial support.

The matrix $\mathcal{A}$ introduced in Equation (9) is given by the following formula:

$$\mathcal{A}=\begin{pmatrix} \exp\frac{-i\omega l^-}{u_0^-+c_A^-} & \exp\frac{-i\omega l^-}{u_0^--c_A^-} & 0 & 0 & 0 & 0 \\ 1 & 1 & -1 & -1 & 0 & 0 \\ u_0^-+c_A^- & u_0^--c_A^- & -u_0^c-c_A^c & c_A^c-u_0^c & 0 & 0 \\ 0 & 0 & \exp\frac{i\omega L}{u_0^c+c_A^c} & \exp\frac{i\omega L}{u_0^c-c_A^c} & -\exp\frac{i\omega L}{u_0^++c_A^+} & -\exp\frac{i\omega L}{u_0^+-c_A^+} \\ 0 & 0 & \left(u_0^c+c_A^c\right)\exp\frac{i\omega L}{u_0^c+c_A^c} & \left(u_0^c-c_A^c\right)\exp\frac{i\omega L}{u_0^c-c_A^c} & -\left(u_0^++c_A^+\right)\exp\frac{i\omega L}{u_0^++c_A^+} & \left(c_A^+-u_0^+\right)\exp\frac{i\omega L}{u_0^+-c_A^+} \\ 0 & 0 & 0 & 0 & \exp\frac{i\omega(L+l^+)}{u_0^++c_A^+} & \exp\frac{i\omega(L+l^+)}{u_0^+-c_A^+} \end{pmatrix}.$$

The quantities $\mathcal{R}_0^c$ and $\mathcal{R}_L^c$ introduced in Equation (11) are defined by the expressions

$$\mathcal{R}_0^c=\frac{\left(u_0^c-c_A^c-u_0^-+c_A^-\right)\exp\frac{-i\omega l^-}{u_0^-+c_A^-}-\left(u_0^c-c_A^c-u_0^--c_A^-\right)\exp\frac{-i\omega l^-}{u_0^--c_A^-}}{\left(u_0^c+c_A^c-u_0^-+c_A^-\right)\exp\frac{-i\omega l^-}{u_0^-+c_A^-}-\left(u_0^c+c_A^c-u_0^--c_A^-\right)\exp\frac{-i\omega l^-}{u_0^--c_A^-}},$$

$$\mathcal{R}_L^c=\frac{\left(u_0^c+c_A^c-u_0^++c_A^+\right)\exp\frac{i\omega l^+}{u_0^++c_A^+}-\left(u_0^c+c_A^c-u_0^+-c_A^+\right)\exp\frac{i\omega l^+}{u_0^+-c_A^+}}{\left(u_0^c-c_A^c-u_0^++c_A^+\right)\exp\frac{i\omega l^+}{u_0^++c_A^+}-\left(u_0^c-c_A^c-u_0^+-c_A^+\right)\exp\frac{i\omega l^+}{u_0^+-c_A^+}}.$$

REFERENCES

Antolin, P., et al. 2008, ApJ, 688, 669
Aschwanden, M., Alexander, D., & Hurlburt, N. 2000, ApJ, 531, 1129
Belien, A. J. C., Martens, P. C. H., & Keppens, R. 1999, ApJ, 526, 478
Brekke, P., Hassler, D. M., & Wilhelm, K. 1997, Sol. Phys., 175, 349
Cargill, P. J., & Priest, E. R. 1980, Sol. Phys., 65, 251
Cirtain, J. W., et al. 2007, Science, 318, 1580
Craig, I. J. D., & McClymont, A. N. 1986, ApJ, 307, 367
Cushman, G. W., & Rense, W. A. 1976, ApJ, 207, L61
De Groof, A., & Goossens, M. 2002, A&A, 386, 691
De Groof, A., Paes, K., & Goossens, M. 2002, A&A, 386, 681
De Pontieu, B., et al. 2007, Science, 318, 1574
Del Zanna, G. 2008, A&A, 481, L49
Doschek, G. A., Bohlin, J. D., & Feldman, U. 1976, ApJ, 205, L177
Doschek, G. A., et al. 2007, ApJ, 667, L109
Doyle, J. G., et al. 2002, A&A, 396, 255
Doyle, J. G., et al. 2006, A&A, 452, 1075
Erdélyi, R., & Fedun, V. 2007, Science, 318, 1572
Gruszecki, M., et al. 2007, A&A, 469, 1117
Hara, H., et al. 2008, ApJ, 678, L67
Heyvaerts, J., & Priest, E. R. 1983, A&A, 117, 220
Hollweg, J. V. 1984a, ApJ, 277, 392
Hollweg, J. V. 1984b, Sol. Phys., 91, 269
Hollweg, J. V., Jackson, S., & Galloway, D. 1982, Sol. Phys., 75, 35
Ionson, J. A. 1978, ApJ, 226, 650
Ionson, J. A. 1982, ApJ, 264, 318
Kudoh, T., & Shibata, K. 1999, ApJ, 514, 493
Mariska, J. T., & Boris, J. P. 1983, ApJ, 267, 409
Mariska, J. T., & Dowdy, J. F., Jr. 1992, ApJ, 401, 754
McKenzie, J. F. 1970, P&SS, 18, 1
Miles, J. W. 1957, ASAJ, 29, 226
Moriyasu, S., et al. 2004, ApJ, 601, L107
Neupert, W. M., et al. 1992, ApJ, 392, L95
Ofman, L. 2002, ApJ, 568, L135
Ofman, L., & Wang, T. J. 2008, A&A, 482, L9
Okamoto, T. J., et al. 2007, Science, 318, 1577
Orlando, S., Peres, G., & Serio, S. 1995, A&A, 294, 861
Peter, H. 2001, A&A, 374, 1108
Peter, H., & Judge, P. G. 1999, ApJ, 522, 1148
Parker, E. N. 1991, ApJ, 376, 355
Patsourakos, S., Klimchuk, J. A., & MacNeice, P. J. 2004, ApJ, 603, 322
Petrie, G. J. D. 2006, ApJ, 649, 1078
Rottman, G. J., Orrall, F. Q., & Klimchuk, J. A. 1982, ApJ, 260, 326
Terradas, J., et al. 2008, ApJ, 678, 153
Thomas, J. H. 1988, ApJ, 333, 407
Tomczyk, S., McIntosh, S. W., & Keil, S. L. 2007, Science, 317, 1192
Van Doorsselaere, T., Nakariakov, V. M., & Verwichte, E. 2008, ApJ, 676, L73
Winebarger, A. R., et al. 2002, ApJ, 567, L89
Zaqarashvili, T. V., & Murawski, K. 2007, A&A, 470, 353